

Numerical study on wetted and cavitating tip-vortical flows around an elliptical hydrofoil: Interplay of cavitation, vortices, and turbulence

Cite as: Phys. Fluids **33**, 093316 (2021); <https://doi.org/10.1063/5.0064717>

Submitted: 26 July 2021 . Accepted: 06 September 2021 . Published Online: 24 September 2021

Chunmei Xie (谢春梅),  Jinyuan Liu (刘晋源), Jing-Wei Jiang (蒋靖伟),  Wei-Xi Huang (黄伟希), et al.



View Online



Export Citation



CrossMark

Physics of Fluids

SPECIAL TOPIC: Flow and Acoustics of Unmanned Vehicles

Submit Today!



Numerical study on wetted and cavitating tip-vortical flows around an elliptical hydrofoil: Interplay of cavitation, vortices, and turbulence

Cite as: Phys. Fluids **33**, 093316 (2021); doi: 10.1063/5.0064717

Submitted: 26 July 2021 · Accepted: 6 September 2021 ·

Published Online: 24 September 2021



View Online



Export Citation



CrossMark

Chunmei Xie (谢春梅),¹ Jinyuan Liu (刘晋源),¹ Jing-Wei Jiang (蒋靖伟),^{1,2} and Wei-Xi Huang (黄伟希)^{1,a)}

AFFILIATIONS

¹Applied Mechanics Laboratory, Department of Engineering Mechanics, Tsinghua University, Beijing 100084, China

²Advanced Propulsion Technology Research Department, China Marine Development and Research Centre, Beijing 100161, China

^{a)} Author to whom correspondence should be addressed: hwx@tsinghua.edu.cn

ABSTRACT

Cavitation in a tip vortex remains a challenging issue in a variety of engineering problems. In this study, we perform large eddy simulation of wetted and cavitating flows around a stationary elliptical hydrofoil with the cross section of NACA (National Advisory Committee for Aeronautics) 16–20. The Schnerr–Sauer cavitation model is adopted for phase transport. The numerical results are verified by comparing with the experimental measurements. Instantaneous vorticity and pressure in both wetted and cavitating flows are studied. It is found that the cavitation promotes the production of vorticity and increases the boundary layer thickness. To further analyze the influence of cavitation on the tip vortices, each term in the transport equation of enstrophy is examined. In the cavitating flow, the dilatation and baroclinic torque terms are promoted to be equally dominant as the vortex stretching term, while in the wetted flow the stretching term is the only dominant one. The axial and azimuthal velocities in the cavity are smaller than those in wetted tip-vortical flow, while the pressure inside is nearly equal to the constant saturation pressure. A tip vortex model with four regions in cavitating flow is built and compared to the wetted flow model. A weakly meandering motion of the tip vortex is observed in the near field. To study the surface wave behaviors of the tip vortex, the space-time velocity correlation analysis is carried out. The surface wave moves at a speed smaller than the incoming flow. A dominating helical mode is found and is consistent with the analytical and experimental results.

Published under an exclusive license by AIP Publishing. <https://doi.org/10.1063/5.0064717>

I. INTRODUCTION

Vortex cavitation is a commonly occurring phenomenon in engineering practice, especially in rotating machinery. For example, submarine propellers and hydrodynamic turbines are subject to cavitation when they are running at a high speed. The ambient pressure will be reduced as the fluid gets accelerated, and when it is lower than the saturation pressure, the liquid will transit into the gaseous phase. This transition is noted as cavitation. Cavitation could lead to additional noise emission, blade material erosion, or propulsion deficiency for underwater propellers;¹ hence, it is usually unfavored in engineering.

The non-dimensional parameter that characterizes the cavitation process is the cavitation number,

$$\sigma = \frac{p_\infty - p_{\text{sat}}}{\frac{1}{2} \rho_l U_\infty^2},$$

where p_∞ and U_∞ are the free-stream reference pressure and velocity, respectively, ρ_l is the fluid density, and p_{sat} is the saturation pressure

which depends on temperature. The critical cavitation number, at which the first isolated cavitation bubble starts to appear in the flow, is noted as σ_c . One way to predict the critical cavitation number is to assume that the pressure field has a minimum on the surface of the hydrofoil with its value being the saturation pressure. Then we have the pressure coefficient relation,

$$C_{p,\text{min}} = \frac{p_{\text{sat}} - p_\infty}{\frac{1}{2} \rho_l U_\infty^2} = -\sigma_c.$$

Hence, the critical cavitation number has a Reynolds number and an angle-of-attack (AOA) dependence as the pressure coefficient C_p does.

Cavitation occurs in various forms and can be categorized into bubble cavitation, cloud cavitation, sheet cavitation, and tip-vortex cavitation (TVC), according to the location that cavitation occurs and whether the cavitating bubbles merge into a continuum.² TVC is the focus of this study. In an airfoil or hydrofoil flow, the location of local pressure minimum is always near the wingtip and at the trailing line

of one side of the wing. To compensate for the discontinuity in velocity circulation, streamwise vortices form at the wingtips and, therefore, are rolled up when being advected downstream.³ Tip vortex is featured by its elongated shape and the significant pressure difference inside and outside the vortical region. Under proper conditions, the ambient pressure in the vortex core could be lower than the saturation pressure, and TVC would occur consequently. TVC involves the interplay among vortical motion, cavitation, and turbulence. The nonlinear interaction among these three flow features introduces rich flow phenomena and complexity. On the one hand, a strong swirling flow leads to pressure reduction, which embeds cavitation. On the other hand, cavitation creates void volume and alters the turbulent vortical flow as well. The impact of the background vortical motion on cavitation has been well studied,⁴ while the counter-acting mechanism of cavitation on vortex dynamics has not yet been well understood and is the focus of this paper.

Ji *et al.*⁵ studied the interaction of sheet-cavitation and vortex in the flow around a Delft Twist-11 hydrofoil. By analyzing the contribution from each term in the vorticity transport equation, they showed that the vortex dilatation term, which is identically zero in fully wetted flow, has a non-trivial contribution to the vorticity, and its magnitude is comparable to the vortex stretching term. Cheng *et al.*⁶ simulated the tip-leakage flow around a NACA0009 hydro-wing by using large eddy simulation (LES) and analyzed the influence of cavitation on vortices and turbulent kinetic energy. They also stressed that the dilatation term in vorticity transportation is as important as the stretching term. However, in the aforementioned work by Ji *et al.*⁵ and Cheng *et al.*⁶ only the cavitating flow was studied; hence, the quantitative comparison of fully wetted flow and cavitating flow was not attained. In this study, we carried out simulations of both wetted and cavitating flows under the same working conditions to isolate the effect of cavitation. Furthermore, the previous studies emphasized more on sheet cavitation, which is dominated by inertia and the viscous effect can be neglected, but in tip vortex cavitation, the viscous effect dominates the flow in the core of the vortex and determines the minimum pressure inside the core. The impact of cavitation on the vortical flow is expected to be different in TVC than in sheet cavitation.

Besides the vortical structures, cavitation has an impact on the turbulence statistics as well. Ohta and Sugiura⁷ performed direct numerical simulation of cavitating flow in the turbulent boundary layer at the displacement Reynolds number $Re_{\delta^*} = 2000\text{--}2600$. They found that the streamwise vorticity and the skin friction in cavitating flow are lower than those in wetted flow, while the streamwise velocity fluctuation is enhanced. The observation above was explained as when cavitation starts to appear, the empty volume it creates in the field destroys the redistribution mechanism in turbulent kinetic energy transportation, so the amount of energy transfer from the streamwise direction to other directions is reduced. When the cavities corrupt, they destroy the small-scale near-wall streaks which generate the drag. Similarly, Iyer and Ceccio⁸ reported increased streamwise turbulent intensity and decreased cross-stream counterpart in a turbulent shear layer. However, the length scales of the cavities are smaller than those of the boundary layer⁷ and the mixing layer,⁸ while in tip vortex cavitation flow the scales of the cavities are much larger than those of the small-scale turbulent motions. The impact of cavitation on turbulence of relatively smaller scales remains to be examined.⁹

Research on cavitating vortices has often been focused on the inception,^{10–14} while much less work was devoted to fully developed vortex cavitation where the detailed vortical flow is more complicated. Falcão de Campos,¹⁵ van Rijsbergen, and Kuiper¹⁶ measured the velocity field surrounding a developed vortex cavity by using laser Doppler velocimetry. They found that the velocity away from the cavity is identical to that of the non-cavitating vortex. Because of the unsteadiness of cavity, the accurate measurement of velocity near the cavity interface is not reached. The velocity around the cavity interface was then measured by particle image velocity.^{17,18} Their results showed that the azimuthal velocity decreases near the cavity interface compared to the non-cavitating case and reaches its maximum at some distance from the edge of the cavity. In the non-cavitating flow, tip vortices at any streamwise section far enough from the tip have been known to be a q -vortex given by Batchelor.³ This was confirmed by a number of measurements, such as in Devenport *et al.*,¹⁹ among others. There is still a lack of knowledge on the structure of the flow around developed vortex cavities. Especially, the effect of viscosity on a developed vortex cavity is not well established.²⁰ The simple Rankine vortex model was extended to the cavitation version condition by Arndt and Keller.²¹ Although the velocity profile recovered by the Rankine model departs from that in real cavitating flow, the model successfully predicted the possibility of the existence of two flow states under the same condition, namely, the single-phase and two-phase states. More realistic analytical vortex models, such as the Lamb–Oseen model, have been generalized to cavitating flows by Bosschers.⁹ His modified Lamb–Oseen vortex predicted the azimuthal velocity profile reasonably well, albeit that only measurement at one streamwise location is used to tune the model coefficients; hence, the proper length scale of the tip vortices was not discussed. In this work, we would gather a sufficient amount of data from numerical simulations to address the question of scaling.

In addition to the statistical description of the structure of TVC, its turbulent nature is also of great importance. Vortex meandering (or wandering) is a typical feature of wing-tip vortices in which the location of the vortex centerline is fluctuating. The origin and the quantitative characterization of the vortex meandering are two major research subjects.^{22–25} The meandering motion of the vortex was originally thought to be due to free-stream turbulence²⁴ and then to the instability of the vortex core.²⁵ Later on, lots of experimental studies were carried out^{19,22,23,26–30} to measure and analyze this phenomenon. Despite that lots of research have been done, the meandering phenomenon of tip vortex is still a puzzle. Another interesting feature of the tip vortex is its wave-like surface on the cavity, which is related to the dynamics. The dynamics of a vortex cavity have been studied extensively. Recently, Bosschers³¹ and Pennings³² used the analytical formulation and experimental measurements to systematically and carefully analyze the dynamics of the tip-vortex cavity. In Bosschers's work,³¹ a dispersion relation was obtained for a columnar vortex cavity in 3-D axisymmetric inviscid compressible flow with a simple correction of the effect of viscosity. This dispersion relation is validated by comparing with the vortex deformation in experiments of Pennings's.³² In this study, the meandering motion and wave-like surface of the cavity are studied using numerical simulations.

Earlier studies on tip vortex were mostly analytical and experimental. With the growth of the computational power, high-fidelity computation of tip-vortex flows becomes accessible. A numerical

computation can provide more a detailed flow field that is unattainable by measurements and can achieve various working conditions that are not easily met or costly in experiments. Numerical simulations have been proved successful in predicting tip vortex cavitation by various studies and were summarized in the introduction of Asnaghi *et al.*³³ based on the category of numerical methods. They performed LES of the flow around an elliptical NACA662-415 hydrofoil, in wetted and cavitating conditions. By comparing with the experiments, they clearly showed that LES has the capability of accurately predicting the velocity and pressure fields even near the vortex core.

We present an LES of both non-cavitating (wetted) and cavitating flows past a NACA16-020 hydrofoil. Two different LES models have been tested and validated, and then a comparison against experimental data is made. The vorticity, pressure, and enstrophy fields are compared between the wetted and cavitating flows with an emphasis on the influence of cavitation on turbulence and vortices. Then characterization and statistics of the tip vortex in both wetted and cavitating flows are performed, and both conceptual and quantitative models are proposed. Additionally, the meandering feature and the wave-like surface of the tip vortex are analyzed.

II. PROBLEM DESCRIPTION AND NUMERICAL METHODS

A. Problem description

In this paper, a numerical study of both the wetted and cavitating tip-vortical flows around an elliptical hydrofoil is presented. The main objective is to better understand the characteristic of the tip-vortex cavity and its interplay of cavitation, vortices, and turbulence. Considerable insight into the tip vortex cavitation problem including the computational requirements for numerical simulations, the flow pattern, the tip vortex, and cavity properties can be obtained from numerical simulation of tip-vortex flow around stationary elliptical foil.³⁴ Here, a stationary elliptic platform having a NACA16-020 cross section with an aspect ratio of 3 is presented, which is an often-used case in tip-vortex study.^{35–37} The laminar separation bubble will be formed at low angles of attack, which is difficult to resolve. Therefore, the angle of attack of the entire elliptical hydrofoil is chosen to be 10°, which is also used in Hsiao *et al.*³⁷ and Fruman *et al.*³⁶

B. Numerical methods

1. Governing equations

With the homogeneous assumption of the mixture of vapor and water in the cavitating flow, the multiphase fluid components are assumed to share the same velocity and pressure. The conservation equations of mass and momentum for LES can be written as

$$\frac{\partial \rho}{\partial t} + \frac{\partial(\rho \bar{u}_i)}{\partial x_i} = 0. \tag{1}$$

$$\frac{\partial(\rho \bar{u}_i)}{\partial t} + \frac{\partial(\rho \bar{u}_i \bar{u}_j)}{\partial x_j} = -\frac{\partial \bar{p}}{\partial x_i} + \frac{\partial(\bar{\tau}_{ij} + \bar{\tau}_{ij}^{SGS})}{\partial x_j}. \tag{2}$$

The overbar denotes the filtered quantities, $\bar{u}_{i=1,2,3} = (\bar{u}, \bar{v}, \bar{w})$ are the filtered velocity components and \bar{p} is the filtered pressure, $x_{i=1,2,3} = (x, y, z)$ are the Cartesian coordinates, t is the time, and ρ is the mixture density defined in the mass transport modeling section.

Moreover, $\bar{\tau}_{ij}$ is the strain rate tensor and is linearly proportional to the strain rate tensor \bar{S}_{ij} , i.e.,

$$\bar{\tau}_{ij} = 2\mu \bar{S}_{ij},$$

where μ is the dynamic viscosity and

$$\bar{S}_{ij} = \frac{1}{2} \left(\frac{\partial \bar{u}_i}{\partial x_j} + \frac{\partial \bar{u}_j}{\partial x_i} \right).$$

The subgrid-scale (SGS) stress tensor $\bar{\tau}_{ij}^{SGS} = \rho(\bar{u}_i \bar{u}_j - \bar{u}_i \bar{u}_j)$ is modeled as

$$\bar{\tau}_{ij}^{SGS} = 2\mu_t \bar{S}_{ij} - \frac{2}{3} \mu_t \frac{\partial \bar{u}_k}{\partial x_k} \delta_{ij},$$

where μ_t is SGS eddy viscosity and δ is Kronecker delta function.

2. SGS modeling

In this work, different SGS models for LES were tested. For the current problem, the rotation in the tip vortex core is significant. The wall-adapting local-eddy viscosity (WALE) model,³⁸ which is based on the velocity gradient tensor, is able to capture the rotational motion in the tip vortex. As a traditional and widely used SGS model, the Smagorinsky model³⁹ was also tested and presented for comparison. The expressions of both the Smagorinsky and WALE models are given below.

The Smagorinsky subgrid-scale model uses the mixing length hypothesis, i.e.,

$$\mu_t = \rho \Delta_s^2 |\bar{S}|,$$

where $|\bar{S}|$ is the modulus of the strain rate tensor and Δ_s is the length scale or grid filter width defined as

$$\Delta_s = f_d C_s (\Delta x \Delta y \Delta z)^{1/3},$$

with the mesh sizes being $\Delta x, \Delta y, \Delta z$ and a Van Driest damping function f_d .^{40,41} The constant C_s is not universal and is set to be 0.1 in this study.

The WALE model is based on the square of the velocity gradient tensor proposed by Nicoud and Ducros.³⁸ According to the direct numerical simulation of isotropic turbulence, energy is concentrated in the streams where vorticity dominates irrotational strain and energy dissipates in eddies and convergence zones.⁴² To mimic the energy transfer from the resolved scales to the subgrid ones, both the strain and rotation rates are needed in SGS modeling. In this model, the eddy viscosity is expressed as

$$\mu_t = \rho \Delta_w^2 \overline{OP}(\mathbf{x}, t)$$

$$\Delta_w = C_w (\Delta x \Delta y \Delta z)^{1/3},$$

where C_w is the model coefficient and $C_w = 0.544$ is chosen in the present simulations. $\overline{OP}(\vec{x}, t)$ is defined as follows:

$$\overline{OP}(\mathbf{x}, t) = \frac{(S_{ij}^d S_{ij}^d)^{3/2}}{(\bar{S}_{ij} \bar{S}_{ij})^{5/2} + (S_{ij}^d S_{ij}^d)^{5/4}},$$

with

$$S_{ij}^d = \bar{S}_{ik}\bar{S}_{kj} + \bar{\Omega}_{ik}\bar{\Omega}_{kj} - \frac{1}{3}\delta_{ij}[\bar{S}_{mn}\bar{S}_{mn} - \bar{\Omega}_{mn}\bar{\Omega}_{mn}]$$

$$\bar{\Omega}_{ij} = \frac{1}{2}\left(\frac{\partial\bar{u}_i}{\partial x_j} - \frac{\partial\bar{u}_j}{\partial x_i}\right).$$

The eddy viscosity goes naturally to zero near the wall so that neither constant adjustment (dynamical modeling) nor damping function is needed for wall-bounded flows.

3. Mass transport modeling

We frame this study under the transport equation model, where the fluid properties are defined as the volume average of the liquid and gas phases as

$$\rho = \alpha_l\rho_l + \alpha_v\rho_v$$

$$\mu = \alpha_l\mu_l + \alpha_v\mu_v,$$

where α is the phase volume fraction and the subscripts l and v represent the liquid and gas phases, respectively. The liquid phase and the gas phase are both incompressible with constant ρ_l and ρ_v . Neglecting solid impurity and non-condensable gas, the relationship

$$\alpha_l + \alpha_v = 1$$

can be assumed. In the cavitating flows, with the effect of mass transport between two phases, an additional equation for the volume fraction, i.e.,

$$\frac{\partial(\alpha_l\rho_l)}{\partial t} + \frac{\partial(\alpha_l\rho_l\bar{u}_j)}{\partial x_j} = \dot{m}, \tag{3}$$

needs to be solved. The term \dot{m} represents the mass transfer from the gas phase to the liquid phase and is to be modeled for closure. For simulating cavitating flows, the mass transport term in Eq. (3) has to be modeled carefully to properly represent the cavitation process. It is observed that the vortex cavity at the model scale is entirely filled with vapor. In this study, the Schnerr–Sauer (S–S) model^{43,44} was used. This model is based on the assumption that the fluid mixture consists of a continuous liquid phase and a large amount of identical, non-interacting, spherical bubbles, which superpose to form the gas phase. In such case, the Rayleigh–Plesset (R–P) equation for single spherical bubble dynamics,

$$R\frac{d^2R}{dt^2} + \frac{3}{2}\left(\frac{dR}{dt}\right)^2 = \frac{p_B(R) - p}{\rho_l} - \frac{2\gamma}{\rho_l R} - 4\frac{\mu_l}{\rho_l R}\frac{dR}{dt},$$

can be used for modeling. In the above equation, γ is the surface tension between the liquid and gaseous phase, and $p_B(R)$ and p are the pressure inside the bubble and the local pressure in the surrounding liquid, respectively. The R–P equation is not solved directly, but is simplified to generate the S–S model,⁴³ which represents an explicit relation between the pressure difference and the rate of mass transfer. In the R–P equation, the second derivative (which stands for the rapid change), the surface tension, and the viscous effect are neglected to yield

$$\frac{dR}{dt} = \sqrt{\frac{2|p_B(R) - p|}{3\rho_l}} = \sqrt{\frac{2|p_{sat} - p|}{3\rho_l}}.$$

Then the rate of mass transport is expressed in terms of the rate of change of the bubble radius and further the ambient pressure, summarized as in Sauer and Schnerr,⁴³

$$\dot{m} = C_{ss}\frac{3\alpha_v\rho_v}{R}\sqrt{\frac{2|p_{sat} - p|}{3\rho_l}}.$$

C_{ss} is an empirical constant for condensation ($C_{ss} = 1$) or vaporization ($C_{ss} = -1$) process. Note that following Eq. (3), \dot{m} is defined to be positive if the mass is transferred to the liquid phase. This model is a highly simplified one and is used for simulation of the well-developed tip vortex cavitation without considering the inception and collapse stages. In addition, the non-condensable gas component is neglected. Thus, the gas and liquid phases in this model are assumed to be incompressible.

4. Computational setup

In this study, the software STAR-CCM+⁴⁵ is used for carrying out the numerical simulations. The finite volume method based on the unstructured mesh is adopted. A second-order bounded-central scheme is applied for spatial discretization, and a second-order implicit scheme is adopted for temporal discretization. The computational domain is shown in Fig. 1. The streamwise, spanwise, and normal directions are denoted as x , y , and z , respectively. The origin of coordinates locates at the center of the root chord of the hydrofoil. The chord length at the root of the hydrofoil is denoted as C , and it is selected as the reference length. The hydrofoil is located in a channel with a height of $3C$, a width of $3C$, and a length of $10C$. The inlet is placed approximately $3C$ upstream of the root chord center and the outlet is placed $7C$ downstream, to eliminate the effect of the computational boundaries. The center of the root is placed in the middle of the computational domain in the normal direction and at the bottom of the computational domain in the spanwise direction. The uniform inflow velocity and static pressure are set at inlet and outlet, respectively. Meanwhile, the zero normal gradient condition is adopted for the velocity at the outlet and the pressure at the inlet, and the symmetry conditions are adopted at other boundaries. In addition, a no-slip condition is set for the hydrofoil surface.

5. Grid generation and refinement

The vortex roll-up and transport involve the flow structures of very small scales, in which the scale of the vortex core is about the same as the boundary layer. Meanwhile, the gradients of pressure and

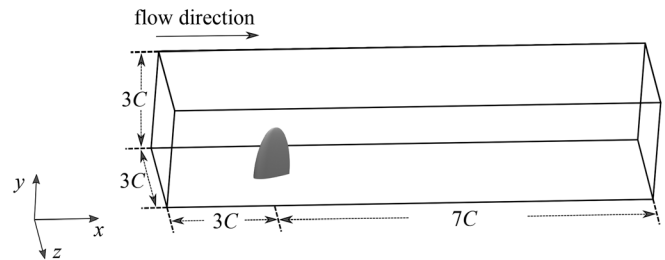


FIG. 1. Schematic of the computational domain.

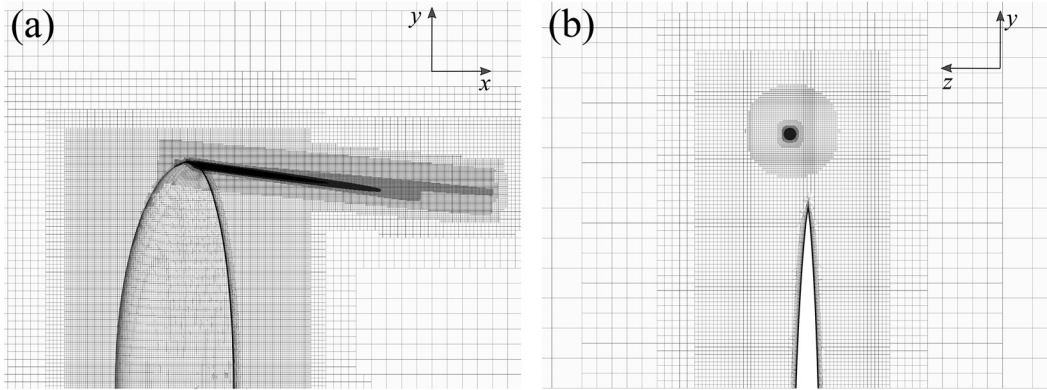


FIG. 2. Mesh around the hydrofoil: (a) a slice cut at $z = 0$ and (b) a slice cut at $x/C = 0.3$.

velocity are very steep in the core region.^{3,46,47} Even a small amount of numerical dissipation will damp these small scales and lead to an incorrect prediction of vortex properties. Therefore, in tip-vortex cavitation simulation, the mesh quality and grid resolution are very important. In Asnaghi *et al.*,³³ they carefully examined the effect of different extents of grid refinement on the resolved flow field and concluded that in order to resolve the large radial gradient near the vortex center, at least 16 grid points are required along the vortex core diameter. This rule will be followed in our grid generation.

An unstructured mesh with mostly hexahedral cells in the field and quadrilateral cells on the body surface is generated as seen in Fig. 2. A total of 8.4 million cells were created. The grid has been refined such that at least 16 grid points are placed in the crosswise direction within the vortex core in the near field. For determining the grid resolution, a coarse mesh without the refinement of the tip-vortex region is generated at the first step. Then, the flow is simulated to find an approximate tip vortex trajectory. Prior refinement zone can be made according to the tip vortex trajectory. Repeat the simulation and find the new approximate tip vortex trajectory that is finer than the last simulation. Then another refinement cylindrical region is made. After several iterations, as shown in Fig. 2, three cylindrical regions are considered around the trajectory path to specify the mesh resolution, having $10^{-2}C$ for the outer refinement cylinder, $5 \times 10^{-3}C$ for the middle refinement cylinder, $8 \times 10^{-4}C$ for the inner refinement cylinder, respectively. As the objective is to study the tip vortex in the near-field region, the cylindrical refinement regions are extended to $2.0C$, $2.0C$, $1.5C$, respectively. The cell distributions in the stream-wise and normal directions are presented in Figs. 2(a) and 2(b), respectively. The first grid above the hydrofoil surface is located at $y^+ \approx 1$ for satisfying the requirement of the wall-resolved LES.

III. RESULTS AND DISCUSSION

The test cases were conducted at a Reynolds number of 4.75×10^6 , which is defined as $Re = \rho_l U_\infty C / \mu$, corresponding to an inlet velocity of $U_\infty = 4.77$ m/s and $C = 1$ m. The dynamic viscosity μ is chosen to be 1.0016×10^{-3} Pa · s corresponding to fresh water at a temperature of 20° Celsius. The density of the liquid is 998.2 kg/m³ and the vapor pressure is 2339.3 Pa.⁴⁸ For the cavitating flow, the vapor density is 0.01731 kg/m³ and the dynamic viscosity is

9.72×10^{-6} Pa · s. The outlet condition is set to $P = 22\,945$ Pa, which corresponds to the cavitation number $\sigma = 1.8$. The simulations are run for more than $10C/U_\infty$ to reach the statistically steady state, and the sequential flow fields spanning about $2C/U_\infty$ thereafter are used for analysis.

A. Numerical validation

The effects of the SGS models are investigated, and the results are compared to the previous experimental measurements.³⁶ As shown in Fig. 3, the axial and azimuthal velocity components across the tip vortex core at $x/C = 0.1$ and 0.3 of the present numerical results are compared with the experimental measurements. It is seen that the tip vortex velocity profiles are well predicted in the near field. LES with the WALE model is more accurate than the Smagorinsky model in the

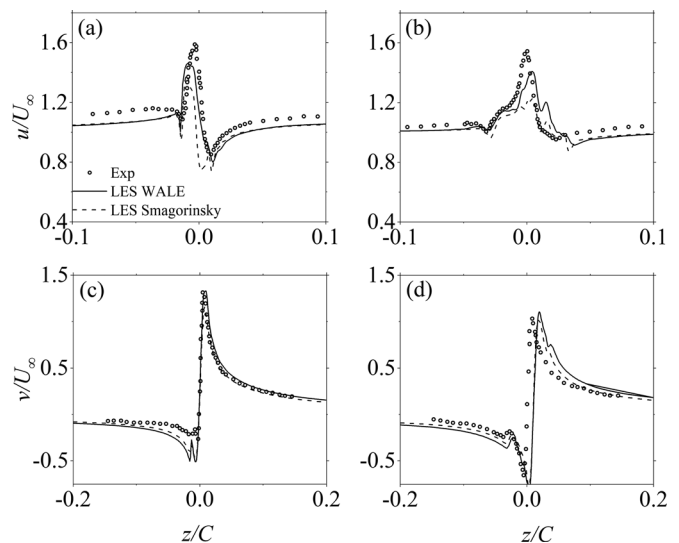


FIG. 3. Comparison of the velocity profiles of the present numerical simulation and the experiment by Fruman *et al.*:³⁶ (a) u/U_∞ at $x/C = 0.1$, (b) u/U_∞ at $x/C = 0.3$, (c) v/U_∞ at $x/C = 0.1$, and (d) v/U_∞ at $x/C = 0.3$.

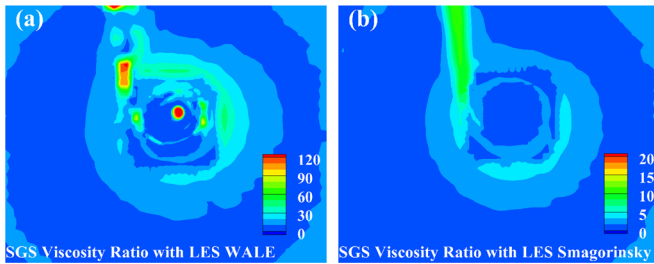


FIG. 4. Contours of the SGS eddy viscosity ratio μ_t/μ at $x/C = 0.3$: (a) WALE model and (b) Smagorinsky model.

vortex core region. In the Smagorinsky model, over-diffusive and dissipative errors are seen further downstream. The SGS eddy viscosity in the WALE model related to both the strain rate tensor \bar{S}_{ij} and rotation rate tensor $\bar{\Omega}_{ij}$, while that in the Smagorinsky model is only related to \bar{S}_{ij} . It results in a different performance in predicting the velocity in the tip vortex core. The SGS eddy viscosity ratio μ_t/μ in the tip vortex at $x/C = 0.3$ is displayed in Fig. 4, in which μ_t/μ in tip vortex core is larger for the WALE model than the Smagorinsky model, due to the fact that the flow is rotating in the vortex core, which is also analytically proved by Phillips.⁴⁹ In this case, the WALE model is better for simulating the turbulent tip vortex flow and is used in the following simulations.

B. Pressure, vorticity, and enstrophy

Simulations of the tip vortex flow with or without cavitation are performed. Significant differences between the results in wetted and cavitating flows are found. It is well acknowledged that vortical flows with strong rotation diminish the ambient pressure and hence initialize cavitation. On the other hand, how cavitation alters the flow remains unclear. To study the effects of cavitation in a tip vortex flow, the vorticity, pressure, and enstrophy are analyzed.

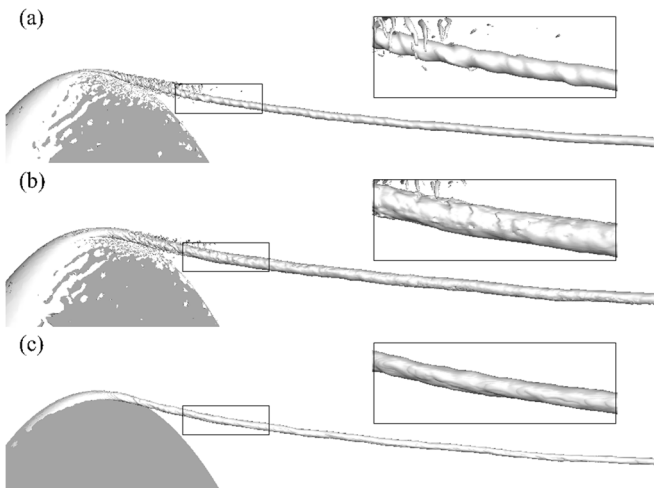


FIG. 5. Wave-like surface on the tip vortex and cavity core: (a) the iso-surface of QC^2/U_∞^2 of a value 2000 in wetted flow, (b) the iso-surface of QC^2/U_∞^2 of a value 2000 in cavitating flow, and (c) the iso-surface of $x_v = 0.1$ in cavitating flow.

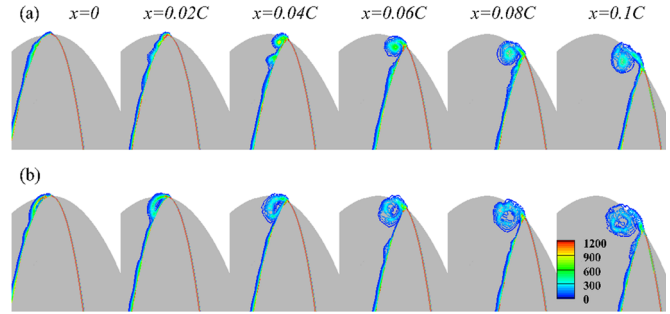


FIG. 6. Contours of the non-dimensional vorticity $|\omega|C/U_\infty$ in the very near field at different streamwise locations: (a) wetted flow and (b) cavitating flow.

To visualize the tip vortex core and the cavity core, the iso-surfaces of Q criteria⁵⁰ and the volume fraction of gas are used. The iso-surface of Q non-dimensionalized by U_∞^2/C^2 for both wetted flow and cavitating flows can be observed in Figs. 5(a) and 5(b), respectively. The tip vortex rolls up from the pressure side to the suction side of hydrofoil and a small part of vortex attached on the tip of hydrofoil in Fig. 5(a), while in Fig. 5(b), due to the cavitation, the tip vortex core is larger than that in wetted flow and a much larger part attached on the tip of hydrofoil. The wave-like surface of the tip vortex is found in both wetted and cavitating flows. This feature can be observed clearly in the insets of Figs. 5(a) and 5(b). The wave-like behavior in Fig. 5(a) is more clear than that in Fig. 5(b). The iso-surface of volume fraction of gas is plotted in Fig. 5(c). The core of the cavitation is smaller than the tip vortex in the cavitating flow. A more ordered wave-like surface can also be observed in the inset of Fig. 5(c) than that of Fig. 5(b). To further understand the structure and mechanism of tip vortex and cavity, the instantaneous vorticity and pressure fields are illustrated in Figs. 6 and 7, respectively. The vorticity field in the very near field at $x = 0-0.1C$ in the wetted flow is plotted in Fig. 6(a) and in the cavitating flow is shown in Fig. 6(b). The vorticity from upstream to downstream in Fig. 6(a) shows that the main vortex arises from the rolling-up process at $x = 0.04C$, and then it transports to the downstream with continuously supplying of vorticity from the boundary layer. At $x = 0.06C$ and $0.08C$, the secondary vortex is built and is merged to the main vortex. Because of the specific location of these two vortices, the secondary vortex deforms the main vortex, making it more elliptical than circular. The vorticity in cavitating flow in Fig. 6(b) shows

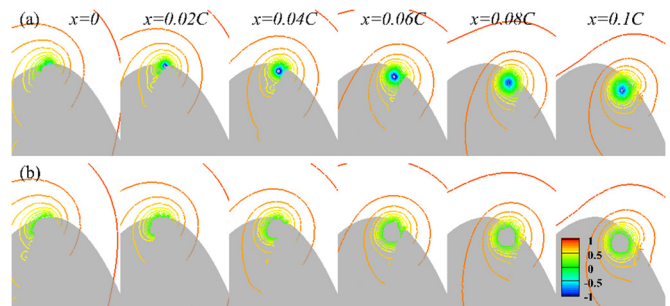


FIG. 7. Contours of the non-dimensional pressure $p/(\rho U_\infty^2)$ in the very near field at different streamwise locations: (a) wetted flow and (b) cavitating flow.

that the cavity has a large influence on the tip vortex. Unlike in Fig. 6 (a), the vorticity is already strong on the tip of the hydrofoil at $x = 0$. At $x = 0.02C$, a distinct cavitation section is observed and the main vortex is presented. As transporting downstream, the main vortex becomes larger and larger with a circular cavity inside the vortex. The secondary vortex arises at $x = 0.06C$ and $0.08C$, which is merged to the main vortex along with the outside circular vortex of the cavity. It can be confirmed that the cavitation promotes vorticity production and increases the boundary layer thickness with local separation.

The pressure in the near field in wetted and cavitating flows is plotted in Figs. 7(a) and 7(b), respectively. As the vortices transport from upstream to downstream, the strength of pressure at the center of the tip vortex becomes larger and then smaller, while the core region seems to become larger and then keep constant in wetted flow, as seen in Fig. 7(a). The pressure in the cavity core is very small compared to the tip vortex core in the wetted flow, as seen in Fig. 7(b). The pressure in the outer tip vortex core is similar for both the wetted and cavitating flows.

With the mass transfer and the density difference near the two-phase interface, the dilatation term and baroclinic torque term also contribute to the generation of vorticity ($\omega = \nabla \times \mathbf{u}$). To quantify these effects, we calculated the budget terms in the enstrophy transport equation,

$$\frac{D\omega^2/2}{Dt} = \omega\omega : \nabla\mathbf{u} - \omega^2(\nabla \cdot \mathbf{u}) + \omega \cdot \frac{\nabla\rho \times \nabla p}{\rho^2} + \nu_{\text{eff}}\nabla^2(\omega^2/2) - \nu_{\text{eff}}\nabla\omega : \nabla\omega, \quad (4)$$

where $\nu_{\text{eff}} = (\mu + \mu_t)/\rho$. The terms on the right-hand side represent the stretching, dilatation, baroclinic torque, and viscosity (diffusion and dissipation) terms, respectively, and are plotted in Fig. 8, left for the wetted flow and right for the cavitating flow. As shown in the left column of Fig. 8, the stretching term is the dominating term while the viscosity term remains small. As expected, the dilatation term is zero due to incompressibility, and the baroclinic torque term is zero

because of the constant density in the whole domain. For the cavitating flow, the dilatation term and the baroclinic torque term dominate as the stretching term does. These two terms related to the density change and compressibility are concentrated only on the interface of phase change. The stretching and viscosity term are smeared and surrounding the cavity core. It is noted that these observations are different as compared to those of Ji *et al.*⁵ In their simulation of flow around a twisted hydrofoil, the stretching and dilatation terms are dominating, while the baroclinic torque and viscosity terms are quite small.

C. Tip vortex models

When the cavitation occurs, it was observed that the flow pattern in the tip vortex changes significantly in Fig. 5. In this section, we analyze in detail the flow structure of the tip vortices. Planar visualizations of the contours of Q of the averaged wetted and cavitating flows at the streamwise location $x = 0.3C$ are shown in Fig. 9.

It can be seen in Fig. 9 that the vortex core can be clearly defined as the red region with the compact positive Q where the rotation dominates the shear, in both the wetted and cavitating cases. The vortex core region is separated from the surrounding region in blue with the negative Q by a sharp interface, which corresponds to the viscous radius r_ν . Actually, the viscous radius can be further defined as the location of the radial maximal azimuthal velocity, which indicated the region within which the viscosity takes effect. Additionally, the shape of the vortex core is fairly circular after time averaging, but in instantaneous fields, the vortex cores are twisted instead. We will discuss more in-depth the variation of the size and location of the vortex core in the later section.

The observation of vortical structure in Fig. 9(a) agrees qualitatively well with the tip vortex model in the wetted flow proposed by Phillips⁴⁹ and Bosschers,²⁰ where the vortex is divided into four regions from inside to outside: (I) rigid-body rotation region, (II) turbulent viscous region, (III) roll-up and merged region, and (IV) potential flow region, as depicted in Fig. 10(a). In the region I, the pressure

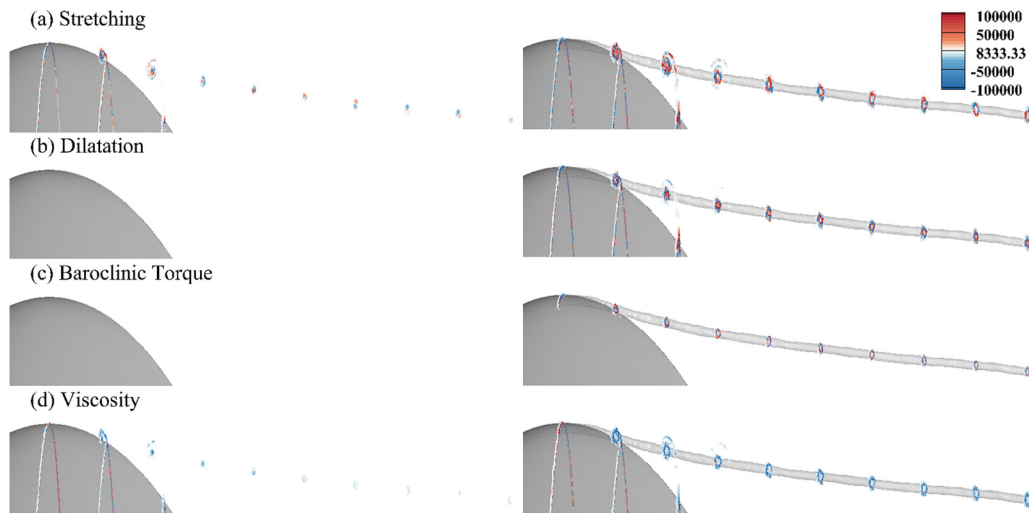


FIG. 8. Contours of the budget terms of the enstrophy transport equation, non-dimensionalized by U_∞^3/C^3 , in the left column for wetted flow and in the right column for cavitating flow: (a) stretching term, (b) dilatation term, (c) baroclinic torque term, and (d) viscosity term. The slice cuts are located at $x = 0-0.9C$. The iso-surface of $\alpha_v = 0.1$ in cavitating flow is also plotted in the right column.

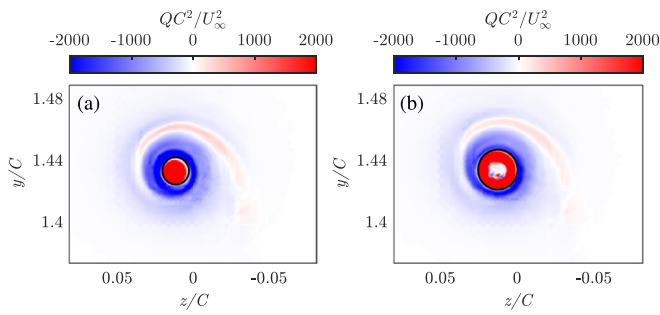


FIG. 9. Distribution of QC^2/U_∞^2 for the time-averaged flow field: (a) wetted flow and (b) cavitating flow. The black solid circles indicate the radii of maximal azimuthal velocity. The cross-sections are taken at the streamwise location $x = 0.3C$, with a perspective from rear to front.

is reduced due to the rotation and the gradient of azimuthal velocity is very large; in the region II, turbulence and viscosity affect the fluid, and the maximum azimuthal velocity is inside this region; the vortex rolls up and merges to the inside region in the region III; in the region IV, the viscous effect is negligible. These four regions are shown clearly in Fig. 9—the regions I and II are marked by the dark red and blue region with intense values of Q , while the regions III and IV are shown by the roll-up layers with Q of alternative signs.

The main difference in Figs. 9(a) and 9(b) is within the regions I and II. When the cavitation occurs, the gaseous region appears at the center of the vortex; hence, the size of the regions I and II are enlarged due to the displacement effect. As a consequence, the size of the vortex core noted by the viscous diameter r_v is increased in the cavitating flow. However, the outer parts are nearly unchanged. Following the model in Fig. 10(a) and combining the observation in Fig. 9, a conceptual model is proposed for cavitating tip vortex as depicted in Fig. 10(b). The cavitating vortex model shares the same feature as that in Fig. 10(a), with four distinct regions marked as I–IV, albeit that the radii of each region are altered. Region I expands while the regions II and III shrinks, as compared with those in Fig. 10(a).

Figure 11 shows the profiles of instantaneous velocity and pressure at $x/C = 0.1$ for wetted and cavitating flows. This location is chosen not to be too close to the wingtip so that the effect of shedding boundary layer is eliminated and the tip vortices are developed. The results at other downstream locations also have the similar characteristics. As shown in Fig. 11, the instantaneous radial and azimuthal velocities are not axisymmetric as the tip vortex is not circular due to the

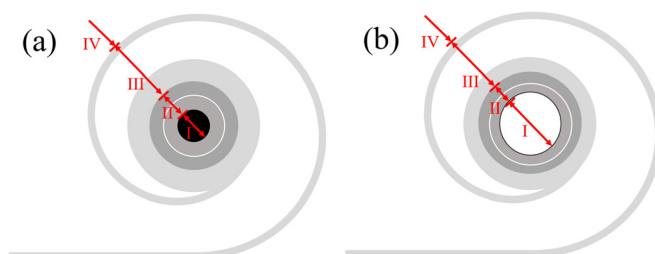


FIG. 10. Tip vortex models showing the roll-up of the vortex sheet and the different flow regions: (a) wetted flow and (b) cavitating flow. The white solid circle within region II indicates the diameter r_v of the viscous core.

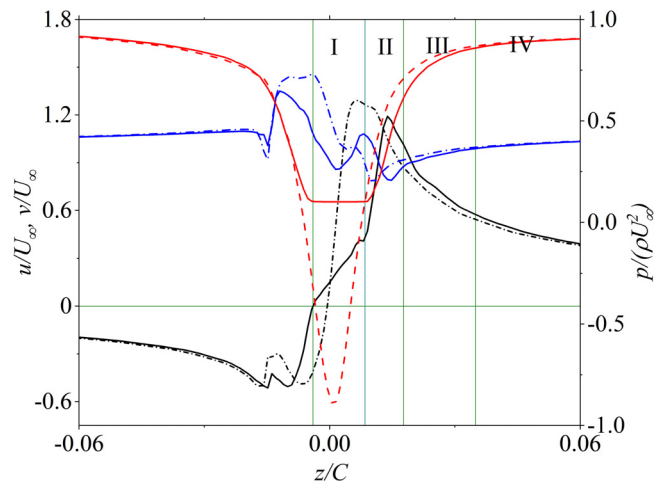


FIG. 11. Comparison of instantaneous velocity and pressure profiles at $x/C = 0.1$ in wetted and cavitating flows. The dashed lines represent the quantities in wetted flow and the solid lines represent the ones in cavitating flow. The blue lines are u/U_∞ ; the black lines are v/U_∞ ; and the red lines are pressure $p/(\rho U_\infty^2)$.

vortex roll-up effect. For instance, the velocity deficit of v near $z/C = -0.01$ is due to the spiral arm of the vortex sheet. However, we separate different flow regions in this study according to the radius for the sake of simplicity. The vertical green lines in Fig. 11 show the four regions of the tip vortex model in the cavitating flow. Region I is a cavity region with a quasi-constant pressure. According to Fig. 11, this cavity edge is slightly larger than that of maximal azimuthal velocity, and a significant difference between wetted and cavitating flows can be seen in the regions I and II. The axial velocity in the core of vortex in wetted flow is driven by the axial pressure gradient $\partial p/\partial x$, which depends on the growth of vortex core, the gain in circulation in the roll-up process, and the effects of the boundary layer.³ When the cavitation is present, the core pressure is nearly equal to the vapor pressure, and the axial pressure gradient is, therefore, reduced in this region. This leads to the suppression of the axial velocity in the region I of the cavitating flow. Similarly, the radial velocity gradient $\partial p/\partial r$, which balances the centrifugal acceleration $\rho u_\theta^2/r$, is also reduced in the cavitating flow, resulting in a more quiescent circumferential flow in region I. Discontinuity of the radial gradient of azimuthal velocity close to the edge of cavity is found. It is caused by the non-zero mass transfer between the two phases, which was also presented in Ref. 51.

In the analysis above, we build up a qualitative model for the tip vortex. In the following, we pursue the scaling law of the azimuthal velocity and show its relation to the classical vortex models. In Fig. 12, we scale the time-averaged azimuthal velocity profile at different locations ranging from $x = 0.5C$ to $x = 1.0C$ in both the wetted and cavitating flows against the combined spatial coordinate $z/\sqrt{x}C$. Note that the vortices are centered at different positions at different streamwise locations, so we shift individual velocity profiles in Figs. 12(a) and 12(b) so that their origins coincide.

Azimuthal velocities at different streamwise locations collapse well for both wetted and cavitating flows, especially in the inner regions I and II dominated by viscosity. This implies a similarity of the velocity viewed in the combined coordinate $z/\sqrt{x}C$. It is also shown

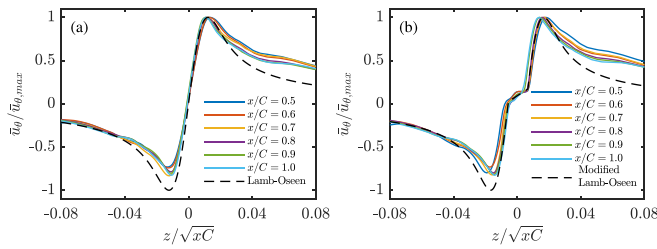


FIG. 12. Distribution of time-averaged azimuthal velocity in (a) wetted and (b) cavitating flow. The horizontal axis is normalized by the chord length C and the streamwise coordinate x . The vertical axis is normalized by the maxima of each line.

that the velocity profiles in Fig. 12(a) agree with the Lamb–Oseen vortex model up to the region II. The Lamb–Oseen model is given by

$$u_\theta = \frac{\Gamma}{2\pi r} \left(1 - e^{-\frac{r^2}{r_\nu^2}}\right), \quad r_\nu = 2\sqrt{\nu t_\nu}, \quad (5)$$

where Γ is the circulation, and the length scale r_ν is the viscous radius representing the region that viscosity can affect at time t_ν . It is shown in Fig. 12(a) that the temporally evolving Lamb–Oseen vortex is related to the spatially developing tip vortices by marching the characteristic viscous timescale as

$$t_\nu = x/U, \quad (6)$$

where x is the streamwise coordinate. Then the length scale of the viscous radius becomes

$$r_\nu = \sqrt{xC}, \quad (7)$$

which is the length scale used in Fig. 12. This analogy is valid only if the motion of the tip vortex can be decoupled into streamwise advection and planar diffusion. In other words, the tip-vortical motion can be viewed as a planar diffusion in a reference frame traveling with the background convection velocity and along the trajectory of the vortex core. This is confirmed by Fig. 12(a) where the velocity profiles collapse well when the spatial coordinate z is scaled with \sqrt{xC} in the range of $x/C = 0.5$ – 1.0 . It is checked that this agreement cannot be achieved by scaling z with x , and the azimuthal velocities at $x \leq 0.5C$ do not have this scalable property, presumably because the similarity is not established yet too close to the wingtip. Also, the spatial resolution restricts us from making an accurate comparison in the far wake.

In Fig. 12(b), the change introduced by cavitation is modeled into the modified Lamb–Oseen vortex model by displacing and re-scaling the viscous core region as

$$u_\theta = \begin{cases} ar, & 0 \leq r \leq r_c \\ \frac{\Gamma}{2\pi r'} \left(1 - e^{-\frac{r'^2}{r_\nu^2}}\right), & r' = (r - r_d) \quad r \geq r_c, \end{cases} \quad (8)$$

where r_c is the radius of cavitation core and r_d is the effective displacement radius. This is again a reflection of the fact that the kinematic effect of cavitation is to displace the vortex core outward, but without changing the velocity in the outer regions. The velocity profile given by Eq. (8) is plotted in Fig. 12(b) for comparison, with $a \approx 25.4$.

However, both the original and modified Lamb–Oseen models under-predict the velocity out of the viscous region, which can be seen

from the discrepancy between the numerical results (solid lines) and the simplified model (dashed lines) in Figs. 12(a) and 12(b), especially at $z > 0$. The difference is, on the one hand, due to the spiral shape of tip vortices, which does not exactly match the axisymmetry assumption in Lamb–Oseen’s model. On the other hand, the Lamb–Oseen model is a laminar model, which does not take into account the effect of turbulence diffusion.

D. Meandering motion

In the previous sections, vortex models are built in the sense of the average flow, but the actual tip-vortical flow is developing in space and fluctuating in time. To characterize this non-uniform and unsteady features, we separate the fluctuation and the base flow of the tip vortex. In this section, we focus on the fluctuations of the vortices at specific streamwise sections, while the spatial-temporal correlation will be presented in the next section.

Here, the locations of w_{max} , w_{min} , v_{max} and v_{min} are identified, as shown in Fig. 13. After the tip vortices are well developed, 400 snapshots with a time interval of 0.001 are analyzed. Figure 13(a) shows the results in the wetted flow, and Fig. 13(b) presents the ones in the cavitating flow, in four different downstream locations $0.1C$, $0.3C$, $0.6C$, $1.0C$. According to Figs. 5 and 13, the vortex is directed to the suction side and the root of the hydrofoil. The shift of the vortex core in the y -direction is more evident than in the z -direction. As expected, at a certain streamwise cross section, the vortex core sizes in cavitating flow shown in Fig. 13(b) are larger than those in the wetted flow in Fig. 13(a) because of the presence of the cavity. The distributions of maximum and minimum velocities seem to tend to align more cohesively near the circle further downstream. The change of locations of w_{max} , w_{min} , v_{max} and v_{min} in time is stronger near the tip than in further downstream, and it has different preference in the wetted and cavitating flows. In the cavitating flow, the variation of the velocity maxima is nearly tangent to the circular cavity as shown in Fig. 13(b), while the variation in the wetted flow moves normally to the tip vortex edge shown in Fig. 13(a). We can say that this difference is due to the secondary vortex found in the cavitating case which is rolled-up and supplies vorticity into the region II. The enhanced rotational motion presumably dominates other variations in the cavitating case and leads to stronger fluctuations in the circumferential direction than in the radial direction. To further analyze quantitatively the geometry of the tip vortices and the impact of

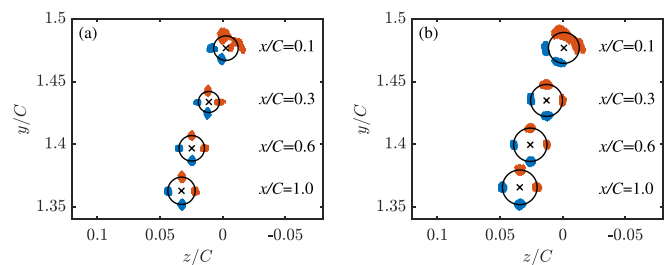


FIG. 13. Locations of w_{max} , w_{min} , v_{max} , and v_{min} : (a) wetted flow and (b) cavitating flow. Squares are the locations of the extrema of v and diamonds are the locations of the extrema of w . Red markers are the maxima and blue markers are the minima. Circles are the circumcircles given by averaged locations of velocity extrema, sorted from top to bottom as $x/C = 0.1, 0.3, 0.6, 1.0$.

cavitation, we calculate the statistics of the sizes and locations for the vortex core as a function of downstream distance in Fig. 14.

Figure 14 shows the variation of vortex core radius and locations as functions of the streamwise coordinate. The center and the radius of a vortex core are defined as the center and the radius of the circumcircle determined by the velocity maxima in Fig. 13. It is evident that the core size of the tip vortex in the cavitating flow is always larger than that in wetted flow at any cross section, and in both cases, the core radius increases slowly downstream. The former result is consistent with our previous argument that the effect of cavitation is to enlarge the viscous radius of vortices. In Fig. 14(b), the locations of the vortex center are compared for the two cases and no significant difference is found, which means that the meandering motion is weak in the near field of both the wetted and cavitating flows. This confirms that the location of the tip vortex is determined by external flow conditions, such as the geometry of the hydrofoil and the inflow conditions, and that the simulation of wetted flow is adequate to predict the location where cavitation is to occur.

E. Wave-like surface

As seen in Fig. 5, the iso-surface of Q in both wetted and cavitating flows has a wave-like feature. To study quantitatively the wavy motion of the tip vortex core, the correlations of velocity in time and in certain downstream locations are analyzed to study the surface wave. The correlation coefficient is expressed as

$$R_{ww}(\Delta t, \Delta x) = \frac{\langle w'(t, x)w'(t + \Delta t, x + \Delta x) \rangle}{\langle w'^2(t, x) \rangle^{1/2} \langle w'^2(t + \Delta t, x + \Delta x) \rangle^{1/2}}. \quad (9)$$

The average $\langle \cdot \rangle$ is defined as the time average and w' is the velocity fluctuation in the normal direction. $R_{ww}(\Delta t, \Delta x)$ with $\Delta t U_\infty / C = (0, 0.4]$ and $\Delta x / C = 0, 0.05, 0.10, 0.15,$ and 0.20 are calculated by using the numerical results at $x = 0.9C, 0.95C, 1.0C, 1.05C, 1.1C$. The results in the wetted and cavitating flows are shown in Figs. 15(a) and 15(b), respectively. With the increasing of Δx , the peaks of R_{ww} move forward like traveling waves. According to Figs. 15(a) and 15(b), the velocity of the surface wave in tip vortex is $U_{sw} / U_\infty = \Delta x C / (\Delta t U_\infty) \approx 0.87$ m/s and smaller than the incoming flow. Comparing the results in the wetted and cavitating flows, the correlations of wetted flow keep better similarity in different Δx than that in

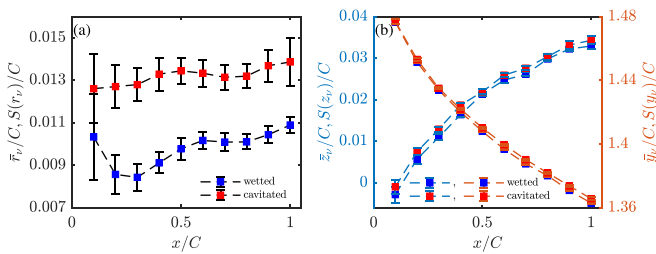


FIG. 14. Spatial description of the tip vortex: (a) vortex core radii and (b) vortex core locations. Statistics is sampled at the streamwise locations ranging from $x/C = 0.1$ to $x/C = 1.0$ with an increment of 0.1 . Time-averages are denoted by the over-bar and plotted as the markers; standard deviation is denoted as $S(\cdot)$ and plotted as the vertical error-bars. Subscript v represents the properties of the viscous cores of vortices. Blue markers are for wetted flow, while red markers are for cavitating flow. In (b), the blue dashed curves are corresponding to the left y -axis while the red curves are corresponding to the right y -axis.

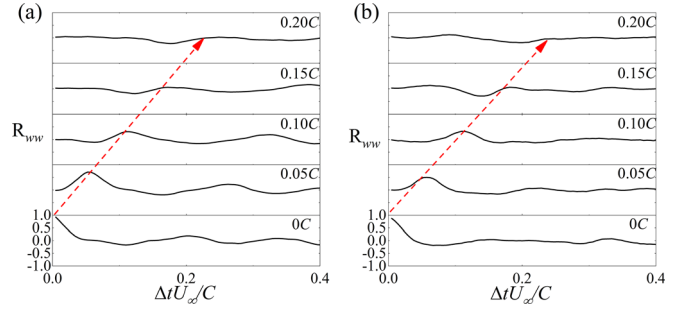


FIG. 15. The correlation coefficient $R_{ww}(\Delta t, \Delta x)$: (a) wetted flow and (b) cavitating flow.

the cavitating flow, which reveals that the cavity causes further complexity in tip vortex. According to Fig. 15, the surface wave has a dominating propagating mode moving with a velocity of $U_{sw} / U_\infty = 0.87$. The non-dimensional frequency of this surface wave is

$$\tilde{\omega} = \frac{2\pi f r_c}{U_\infty} = \frac{2\pi U_{sw} r_c}{\lambda_x U_\infty} \approx 0.24, \quad (10)$$

with a mean cavity radius $r_c = 0.0070C$ and a wavelength $\lambda_x = 0.16C$ from the numerical results.

The numerical results are confirmed by compared to the theory of Bosschers.³¹ The cylindrical coordinates (r, θ, ζ) are used herein and after in the Appendix for analyzing the tip vortex where the ζ -direction is the same as the x -direction in the Cartesian coordinates. From the numerical simulations, the following parameters are measured: the averaged non-dimensional mean axial velocity on the interface of cavity $\bar{u}_{\zeta c} / U_\infty \approx 1.1$, the cavitation number $\sigma = 1.8$, the mean viscous radius $r_v = 0.0136C$, and the mean cavity radius $r_c = 0.0070C$. By substituting these parameters into the dispersion equation, the non-dimensional frequency is plotted for different $\kappa = k_x r_c$ in Fig. 16. It is seen that the non-dimensional frequency of surface wave at $x = 0.9C$ is close to the theoretical results. The results

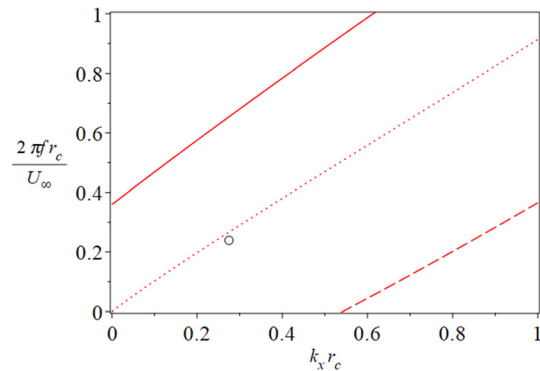


FIG. 16. Non-dimensional dispersion diagram according to the dispersion equation of Bosschers³¹ given in Eq. (A1) in the Appendix for the cavity deformation modes: breathing mode, helical mode, double helix in dashed, dotted, and solid lines, respectively. The black circle represents the present numerical result at $x = 0.9C$.

indicate that the helical mode is the dominating mode, consistent with the experimental results of Pennings,³² as seen in the Appendix.

IV. CONCLUSIONS

In this study, both the wetted and cavitating flows around a stationary elliptical hydrofoil with a cross section of NACA16-020 were simulated to study the tip vortex cavitation problem. To capture the small-scale structure in tip vortex, large eddy simulations with Smagorinsky and WALE models were carried out. A local refinement mesh ensuring 16 grids inside the tip vortex core and a total of 8.4 million cells are used. The numerical setup was validated by comparison with the experimental results. We adopted the Schnerr–Sauer cavitation model for the phase transport modeling. For the case with an angle of attack 10° and $Re = 4.75 \times 10^6$, the numerical results with or without the cavitation model were presented.

Comparing the results of wetted and cavitating flows, it was found that the cavitation induces a boundary layer separation with large increases in the vorticity at the cavity. The axial and azimuthal velocities inside the cavity are smaller than ones in wetted flow. The gradient of pressure inside the cavity is around zero. Unlike the enstrophy in wetted flow in which the stretching term is dominating, the enstrophy term in the cavitating flow is also dominated by the dilatation and baroclinic torque terms.

To describe the tip-vortical flow features, two tip vortex models with and without cavity were built, and a quantitative comparison against the simplified vortex model of Lamb–Oseen was made. We found that the azimuthal velocity profile scales with the combined coordinate z/\sqrt{xC} instead of z/C , and the spatially evolving tip vortex can be transferred to the temporally decaying Lamb–Oseen vortex by marching the characteristic vorticity diffusion timescale $t_\nu = x/U_\infty$. This implies that the swirling motion of the tip vortex is self-similar and can be decomposed into streamwise advection and planar diffusion.

Furthermore, the statistics of the geometry of tip vortices are compared. It was observed that cavitation has a slight influence on the location and shape of the tip vortex. The meandering motion is weak near the tip. Meanwhile, the vortex intensity is increased by cavitation as well, which is owed to the dilatation and baroclinic torque terms in the enstrophy equation.

A velocity correlation analysis of space and time was made. According to the correlation analysis, it was revealed that the tip vortex surface wave moves slower than the incoming flow and the cavity introduces further complexity to the tip vortex. The correlation analysis is verified by comparing with Bosschers’s³¹ and Pennings’s³² work, and the helical mode was found to be the dominating mode.

ACKNOWLEDGMENTS

The work was supported by the National Natural Science Foundation of China under Grants Nos. 11772172 and 91752205. No conflicts of interest.

APPENDIX: DISPERSION EQUATION

To validate our numerical analysis, the analytical dispersion relation for a 3-D columnar vortex cavity³¹ and experimental measurements³² is used. With the assumption of potential flow and

viscous effect correction, the dispersion relation for a 3-D columnar vortex cavity was obtained by Bosscher’s work,³¹ i.e.,

$$\tilde{\omega}^\pm(\kappa, n) = \frac{\omega^\pm r_c}{U_\infty} = \tilde{u}_{\zeta c} \kappa + \tilde{u}_{\theta c} n \pm \sqrt{K_\sigma} \sqrt{\frac{-|\kappa| K'_n(|\kappa|)}{K_n(|\kappa|)}} T_\omega, \quad (A1)$$

where n is the mode number, as seen in Fig. 17. The mode $n = 0$ is a breathing mode and leads to volume variations; the mode $n = 1$ is only related to a displacement of the vortex centerline and named as helical mode; mode $n = 2$ is the double helix mode that involves an elliptical shape of the vortex cross section. The cylindrical coordinate (r, θ, ζ) is more convenient for the analysis of 3-D columnar vortex and is used here. u_θ is the azimuthal velocity of the vortex, and u_ζ is the axial velocity defined same as u_x in this study. $\tilde{\omega}$ is the non-dimensional frequency, $\kappa = k_\zeta r_c = k_x r_c$, and r_c is the mean cavity size. $\tilde{u}_{\zeta c}$ and $\tilde{u}_{\theta c}$ are the non-dimensional mean axial and azimuthal velocity on the cavity edge, respectively. K_σ can be considered as a stiffness term in the non-dimensional form:

$$K_\sigma(\sigma, r_c, r_v) = \sigma \frac{r_c^2}{r_v^2 + r_c^2},$$

with σ is the cavitation number defined with U_∞ , and r_v is the mean viscous tip vortex core. K_n is the modified Bessel function of the second kind with order n , and K'_n is the first derivative of K_n with respect to its argument. T_ω is related to the surface tension. Here, the contribution of surface tension is neglected and $T_\omega = 1$. The mean azimuthal velocity on the cavity edge can be modeled by cavitating Lamb–Oseen vortex, i.e.,

$$\tilde{u}_{\theta c} = \sqrt{\sigma} \sqrt{\frac{r_c^2}{r_v^2 + r_c^2}}.$$

There is no existing model for $\tilde{u}_{\zeta c}$. In Bosschers’s work,³¹ $\tilde{u}_{\zeta c} = 1$ is used.

The modified Bessel function can be simplified for limiting values of the axial wavenumber seen in Ref. 52, and then the dispersion equation (A1) becomes

$$\tilde{\omega}^\pm(\kappa, n) = \tilde{u}_{\zeta c} \kappa + \tilde{u}_{\theta c} n \pm \sqrt{K_\sigma} \sqrt{n}, \quad \forall n > 0, \quad \kappa \ll 1. \quad (A2)$$

When $n = +1^-$, in which the sign symbol in front of 1 corresponds to the first sign symbol in Eq. (A2) and the superscript sign symbol corresponds to the second sign symbol in Eq. (A2), and $\kappa \ll 1$, we have $\tilde{\omega}^\pm(\kappa, n) \rightarrow \tilde{u}_{\zeta c} \kappa$. The non-dimensional frequency $\tilde{\omega}$ only

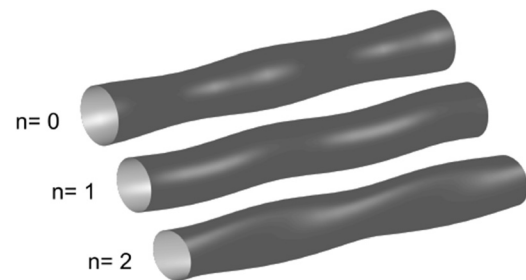


FIG. 17. Deformation modes of the vortex cavity.

TABLE I. Conditions for the cavitation tunnel tests of Pennings³² at an AOA of 7° with a cross section of NACA 662 – 415 and the present numerical simulation at an AOA of 10°, including the mean viscous tip vortex core r_v , mean cavity size r_c , cavitation number σ , tunnel velocity U_∞ , Reynolds number Re based on the chord length at the root C . The non-dimensional mean axial and azimuthal velocities at the cavity interface $u_{\zeta c}$ and $u_{\theta c}$ are also listed.

	r_v (mm)	r_c (mm)	100 r_c/C	σ	U_∞	Re	$\bar{u}_{\zeta c}$	$\bar{u}_{\theta c}$
Present	1.36	0.70	0.70	1.80	4.77	4.75×10^6	1.10	0.61
Case A in Penning's ³²	1.20	0.48	0.38	2.33	6.26	8.95×10^5	1.25	0.4

depends on the axial velocity on the cavity edge $\bar{u}_{\zeta c}$; thus, the helical mode with $n = +1^-$ is also called as a convective line.

The conditions for the experimental cavitation tunnel in Pennings's work³² and the numerical cavitation tunnel in this study are shown in Table I. A stationary elliptical hydrofoil with cross-section NACA 662 – 415 at an AOA of 7° is used.³² The mean viscous tip vortex core r_v , mean cavity size r_c , cavitation number σ , tunnel velocity U_∞ , Reynolds number Re based on the chord length at the root C , and the non-dimensional mean axial and azimuthal velocity at the cavity interface $u_{\zeta c}$ and $u_{\theta c}$ are listed in Table I. The parameters corresponding to the numerical study are also listed. Although the setup of these two cases is different, it is quite similar. The wavenumber-frequency diagram of Pennings's work³² showed that for the case without the singing of vortex, the helical mode, also called as convective line $n = +1^-$, is dominating, while for the singing case, the dominating mode becomes different. Our numerical simulation is consistent with the experimental measurements.

DATA AVAILABILITY

The data that support the findings of this study are available from the corresponding author upon reasonable request.

REFERENCES

- B. H. Maines and R. E. A. Arndt, "Tip vortex formation and cavitation," *J. Fluids Eng. Trans. ASME* **119**, 413–419 (1997).
- R. E. A. Arndt, P. Pennings, J. Bosschers, and T. Van Terwisga, "The singing vortex," *Interface Focus* **5**, 20150025 (2015).
- G. K. Batchelor, "Axial flow in trailing line vortices," *J. Fluid Mech.* **20**, 645–658 (1964).
- R. E. A. Arndt, V. H. Arakeri, and H. Higuchi, "Some observations of tip-vortex cavitation," *J. Fluid Mech.* **229**, 269–289 (1991).
- B. Ji, X. Luo, R. E. A. Arndt, and Y. Wu, "Numerical simulation of three dimensional cavitation shedding dynamics with special emphasis on cavitation-vortex interaction," *Ocean Eng.* **87**, 64–77 (2014).
- H. Cheng, X. Bai, X. Long, B. Ji, X. Peng, and M. Farhat, "Large eddy simulation of the tip-leakage cavitating flow with an insight on how cavitation influences vorticity and turbulence," *Appl. Math. Model.* **77**, 788–809 (2020).
- T. Ohta and R. Sugiura, "Numerical prediction of interaction between turbulence structures and vortex cavitation," *J. Turbul.* **20**, 599–625 (2019).
- C. O. Iyer and S. L. Ceccio, "The influence of developed cavitation on the flow of a turbulent shear layer," *Phys. Fluids* **14**, 3414–3431 (2002).
- J. Bosschers, "An analytical and semi-empirical model for the viscous flow around a vortex cavity," *Int. J. Multiphase Flow* **105**, 122–133 (2018).
- C. T. Hsiao and G. L. Chahine, "Scaling of tip vortex cavitation inception noise with a bubble dynamics model accounting for nuclei size distribution," *J. Fluids Eng. Trans. ASME* **127**, 55–65 (2005).
- J. Choi and S. L. Ceccio, "Dynamics and noise emission of vortex cavitation bubbles," *J. Fluid Mech.* **575**, 1–26 (2007).
- L. Zhang, L. Chen, and X. Shao, "The migration and growth of nuclei in an ideal vortex flow," *Phys. Fluids* **28**, 123305 (2016).
- L. Chen, L. Zhang, X. Peng, and X. Shao, "Influence of water quality on the tip vortex cavitation inception," *Phys. Fluids* **31**, 023303 (2019).
- A. Asnaghi, U. Sverinberg, R. Gustafsson, and R. E. Bensow, "Investigations of tip vortex mitigation by using roughness," *Phys. Fluids* **32**, 065111 (2020).
- J. A. C. Falcão de Campos, "Laser-Doppler velocity measurements on tip vortices in non-cavitating and cavitating conditions," in *Cavitation and Multiphase Flow Forum* (ASME FED, New York, 1992), Vol. 135.
- M. van Rijsbergen and G. Kuiper, "Modeling a cavitating vortex," Proceedings of ASME Fluids Engineering Division Summer Meeting, Vancouver, British Columbia, Canada (1997).
- P. Pennings, J. Westerweel, and T. Van Terwisga, "Flow field measurement around vortex cavitation," *Exp. Fluids* **56**, 1–13 (2015).
- M. Dreyer, J. Decaix, C. Münch-Alligné, and M. Farhat, "Mind the gap: A new insight into the tip leakage vortex using stereo-PIV," *Exp. Fluids* **55**, 1849 (2014).
- W. J. Devenport, M. C. Rife, S. I. Liapis, and G. J. Follin, "The structure and development of a wing-tip vortex," *J. Fluid Mech.* **312**, 67–106 (1996).
- J. Bosschers, "On the dispersion relation of a vortex cavity," in *Proceedings of 10th International Symposium on Cavitation* (ASME, 2018), pp. 853–856.
- R. E. A. Arndt and A. P. Keller, "Water quality effects on cavitation inception in a trailing vortex," *J. Fluids Eng. Trans. ASME* **114**, 430–438 (1992).
- C. Del Pino, J. Lopez-Alonso, L. Parras, and R. Fernandez-Feria, "Dynamics of the wing-tip vortex in the near field of a NACA 0012 aerofoil," *Aeronaut. J.* **115**, 229 (2011).
- C. Roy and T. Leweke, "Experiments on vortex meandering," in *FAR-Wake Technical Report AST4-CT-2005-012238, CNRS-IRPHE*, also presented in international workshop on fundamental issues related to aircraft trailing wakes (CNRS-IRPHE, 2008), pp. 27–29.
- G. Baker, S. Barker, K. Bofah, and P. Saffman, "Laser anemometer measurements of trailing vortices in water," *J. Fluid Mech.* **65**, 325–336 (1974).
- S. Green and A. Acosta, "Unsteady flow in trailing vortices," *J. Fluid Mech.* **227**, 107–134 (1991).
- D. Fabre and S. L. Dizès, "Viscous and inviscid centre modes in the linear stability of vortices: The vicinity of the neutral curves," *J. Fluid Mech.* **603**, 1–38 (2008).
- C. Roy, "Dynamique et Stabilité de Tourbillons Avec Écoulement Axial," Ph.D. thesis (Université de Provence-Aix-Marseille I, 2008).
- S. Bailey and S. Tavoularis, "Measurements of the velocity field of a wing-tip vortex, wandering in grid turbulence," *J. Fluid Mech.* **601**, 281 (2008).
- S. J. Beresh, J. F. Henfling, and R. W. Spillers, "Meander of a fin trailing vortex and the origin of its turbulence," *Exp. Fluids* **49**, 599–611 (2010).
- H. Lee and R. Huang, "Frequency selection of wake flow behind a NACA 0012 wing," *J. Mar. Sci. Technol.* **6**, 29–37 (1998).
- J. Bosschers, "Propeller tip-vortex cavitation and its broadband noise," Ph.D. thesis (University of Twente, 2018).
- P. Pennings, "Dynamics of vortex cavitation," Ph.D. thesis (Delft University of Technology, 2016).
- A. Asnaghi, U. Sverinberg, and R. E. Bensow, "Large Eddy simulations of cavitating tip vortex flows," *Ocean Eng.* **195**, 106703 (2020).
- R. E. A. Arndt, "Cavitation in vortical flows," *Annu. Rev. Fluid Mech.* **34**, 143–175 (2002).
- O. Boulon, J. P. Franc, and J. M. Michel, "Tip vortex cavitation on an oscillating hydrofoil," *J. Fluids Eng. ASME* **119**(4), 752–758 (1997).
- D. Fruman, C. Dugue, P. A. Cerrutti, and P. Briancon-Marjolet, "Tip vortex roll-up and cavitation," Nineteenth Symposium on Naval Hydrodynamics, Seoul, Korea, 10 August (1992).

- ³⁷C. T. Hsiao, G. L. Chahine, and H. L. Liu, "Scaling effect on prediction of cavitation inception in a line vortex flow," *J. Fluids Eng. Trans. ASME* **125**, 53–60 (2003).
- ³⁸F. Nicoud and F. Ducros, "Subgrid-scale stress modelling based on the square of the velocity gradient tensor," *Flow Turbul. Combust.* **62**, 183–200 (1999).
- ³⁹J. Smagorinsky, "General circulation experiments with the primitive equations: I. the basic experiment," *Mon. Weather Rev.* **91**, 99–164 (1963).
- ⁴⁰E. R. Van Driest, "On turbulent flow near a wall," *J. Aeronaut. Sci.* **23**, 1007–1011 (1956).
- ⁴¹E. Balaras, C. Benocci, and U. Piomelli, "Two-layer approximate boundary conditions for large-eddy simulations," *AIAA J.* **34**, 1111–1119 (1996).
- ⁴²A. Wray and J. C. R. Hunt, "Algorithms for classification of turbulent structure," in *Proc. IUTAM Symp. on Topological Fluid Mechanics* (Cambridge University Press, 1990), pp. 95–104.
- ⁴³J. Sauer and G. H. Schnerr, "Development of a New Cavitation Model based on Bubble Dynamics," *ZAMM—J. Appl. Math. Mech./Z. Angew. Math. Mech.* **81**, 561–562 (2001).
- ⁴⁴W. Yuan, J. Sauer, and G. H. Schnerr, "Modeling and computation of unsteady cavitation flows in injection nozzles," *Mec. Ind.* **2**, 383–394 (2001).
- ⁴⁵P. L. M. Siemens, *STAR-CCM+ User Guide Version 15.04* (Siemens PLM Software Inc, Munich, Germany, 2020).
- ⁴⁶J. S. Chow, G. G. Zilliac, and P. Bradshaw, "Mean and turbulence measurements in the near field of a wingtip vortex," *AIAA J.* **35**, 1561–1567 (1997).
- ⁴⁷M. Giuni and R. B. Green, "Vortex formation on squared and rounded tip," *Aerosp. Sci. Technol.* **29**, 191–199 (2013).
- ⁴⁸ITTC Specialist Committee, *ITTC—Recommended Procedures Fresh Water and Seawater Properties* (ITTC, 2011).
- ⁴⁹W. R. C. Phillips, "The turbulent trailing vortex during roll-up," *J. Fluid Mech.* **105**, 451–467 (1981).
- ⁵⁰J. Hunt, A. Wray, and P. Moin, "Eddies, stream, and convergence zones in turbulent flows," in *Proceedings of the Summer Program in Center for Turbulence Research* (Stanford University, 1988), pp. 193–208.
- ⁵¹J. J. Schot, P. C. Pennings, M. J. Pourquie, and T. J. Van Terwisga, "Modelling of tip vortex cavitation for engineering applications in OpenFOAM," in *11th World Congress on Computational Mechanics, WCCM 2014, 5th European Conference on Computational Mechanics, ECCM 2014 6th European Conference on Computational Fluid Dynamics, ECFD 2014* (ICNME, 2014), pp. 4753–4764.
- ⁵²M. Abramowitz and I. A. Stegun, *Handbook of Mathematical Functions with Formulas, Graphs, and Mathematical Tables. National Bureau of Standards Applied Mathematics Series 55. Tenth Printing* (ERIC, 1972).